Bone 121 (2019) 107–115

Contents lists available at ScienceDirect

Bone

journal homepage: www.elsevier.com/locate/bone

Full Length Article

Adaptation of the proximal humerus to physical activity: A within-subject controlled study in baseball players

Stuart J. Warden[a,b,*], Julio Carballido-Gamio[c], Keith G. Avin[a,b], Mariana E. Kersh[d], Robyn K. Fuchs[a,b], Roland Krug[e], Ryan J. Bice[a]

[a] Department of Physical Therapy, School of Health and Human Sciences, Indiana University, Indianapolis, IN, United States of America
[b] Indiana Center for Musculoskeletal Health, Indiana University, Indianapolis, IN, United States of America
[c] Department of Radiology, School of Medicine, University of Colorado Denver, Denver, CO, United States of America
[d] Department of Mechanical Science and Engineering, College of Engineering, University of Illinois at Urbana-Champaign, IL, United States of America
[e] Department of Radiology and Biomedical Imaging, School of Medicine, University of California, San Francisco, San Francisco, CA, United States of America

ARTICLE INFO

Keywords:
Exercise
Internal impingement
Mechanoadaptation
Osteoporosis
Shoulder
SPM

ABSTRACT

The proximal humerus is a common, yet understudied site for osteoporotic fracture. The current study explored the impact of prolonged physical activity on proximal humerus bone health by comparing bone properties between the throwing and nonthrowing arms within professional baseball players. The proximal humerus in throwing arms had 28.1% (95% CI, 17.8 to 38.3%) greater bone mass compared to nonthrowing arms, as assessed using dual-energy x-ray absorptiometry. At the level of the surgical neck, computed tomography revealed 12.0% (95% CI, 8.2 to 15.8%) greater total cross-sectional area and 31.0% (95% CI, 17.8 to 44.2%) greater cortical thickness within throwing arms, which contributed to 56.8% (95% CI, 44.9 to 68.8%) greater polar moment of inertia (i.e., estimated ability to resist torsional forces) compared to nonthrowing arms. Within the humeral head and greater tubercle regions, throwing arms had 3.1% (95% CI, 1.1 to 5.1%) more trabecular bone, as assessed using high-resolution magnetic resonance imaging. Three-dimensional mapping of voxel- and vertex-wise differences between arms using statistical parametric mapping techniques revealed throwing arms had adaptation within much of the proximal diaphysis, especially the posterolateral cortex. The pattern of proximal diaphysis adaptation approximated the pattern of strain energy distribution within the proximal humerus during a fastball pitch derived from a musculoskeletal and finite element model in a representative player. These data demonstrate the adaptive ability of the proximal humerus to physical activity-related mechanical loads. It remains to be established how they translate to exercise prescription to improve bone health within the proximal humerus; however, they provide unique insight into the relationship between prolonged loading and skeletal adaptation at a clinically relevant osteoporotic site.

1. Introduction

The proximal humerus is a common site for osteoporotic fracture [1], with fractures most often occurring as a result of a fall [2,3]. Since not all falls result in fracture there is likely importance of regional bone health, defined as the amount (i.e., mass), distribution (i.e., structure) and properties (i.e., quality) of bone material present. No studies have directly linked proximal humerus bone health with fracture risk; however, proximal humerus bone health predicts ex vivo proximal humerus bone strength [4], declines with age [4–7], and is compromised in individuals with osteoporosis [8]. Further, bone health at distant sites (i.e., hip, spine and wrist) is predictive of proximal humerus bone health [6,7,9,10] and fractures [11–14].

Physical activity may be a means of optimizing proximal humerus bone health. The mechanosensitivity of the skeleton is well established, and the mechanical loading associated with physical activity can be potently anabolic and have lifelong benefits. For instance, we observed the humeral diaphysis within throwing arms of Major/Minor League Baseball (MLB/MiLB) players had nearly double the estimated strength compared their contralateral nonthrowing arms, and that one-half of the bone size and one-third of the bone strength benefits attributed to throwing-related physical activity completed when young persisted lifelong [15]. However, we did not assess the proximal humerus in this previous study.

* Corresponding author at: Department of Physical Therapy, School of Health and Human Sciences, Indiana University, 1140 W. Michigan St., CF-120, Indianapolis, IN 46202, United States of America.
E-mail address: stwarden@iu.edu (S.J. Warden).

https://doi.org/10.1016/j.bone.2019.01.008
Received 22 October 2018; Received in revised form 18 December 2018; Accepted 7 January 2019
Available online 08 January 2019

A number of previous studies have explored the influence of physical activity on proximal humerus bone health using racquet sport players as a within-subject controlled model [16–21]. Comparing side-to-side differences (i.e., bilateral asymmetry) between racquet and contralateral non-racquet arms, Kannus and colleagues [16,17,19–21] observed the racquet arm to have 14–16% greater bone mass within the region of the surgical neck of the proximal humerus. However, data were limited to areal dual-energy x-ray absorptiometry (DXA)-derived outcomes, with the exception of the peripheral quantitative computed tomography (pQCT) data provided by Haapasalo et al. [18]. DXA has known limitations when determining the skeletal benefits of physical activity [22].

The aim of the current study was to explore the impact of prolonged physical activity on proximal humerus bone health by comparing differences in bone properties between the throwing and nonthrowing arms of MLB/MiLB players. Bone properties were assessed using a range of imaging and analysis techniques including: 1) areal-based DXA to assess whole proximal humerus bone mass and allow comparison of adaptation to previously published data in racquet sport players; 2) volumetric-based quantitative computed tomography (QCT) to assess bone mass and structure at the level of the surgical neck; 3) magnetic resonance (MR) imaging to assess trabecular bone properties within the humeral head and greater tubercle; and, 4) voxel- and vertex-based techniques to spatially quantify bone density and cortical bone thickness distribution in the proximal humerus using QCT. The spatial assessment of bone health is important as bone loading and adaptation occurs focally within specific tissue regions [23,24] and focal alterations in bone health can distinguish between different types of osteoporotic fracture [23–25].

In addition to bone health assessments, we also calculated strain energy distribution within the proximal humerus during a fastball pitch in a preliminary subject using a subject-specific musculoskeletal model of the upper limb and QCT-based finite element model of the humerus. The strain energy data were used to explore whether the focal regions showing adaptation in the throwing arm corresponded with those loaded. We also explored the functional benefit (i.e. reduction in tissue level loading) of adaptation by comparing strain energy in the throwing arm to that in the nonthrowing (i.e. non-adapted) arm when the same forces were applied.

2. Methods

2.1. Study design and participants

A within-subject controlled cross-sectional study design was used to compare bone properties at the bilateral proximal humeri in male MLB/MiLB baseball players. Subjects were eligible to participate if they: 1) were aged 18–30 years; 2) play MLB/MiLB [Triple-A level] as a pitcher or catcher; 3) begun playing baseball prior to 8 years of age, and; 4) have not had a hiatus from competitive baseball for > 12 months at any time. Exclusion criteria were: 1) known metabolic bone disease; 2) history of a humeral fracture or stress fracture; 3) implanted metal within the proximal humerus, and; 4) exposure to upper extremity immobilization for > 2 weeks within the past 2 years. The study was approved by the Institutional Review Board of Indiana University and written informed consent was obtained from all participants.

2.2. Dual-energy x-ray absorptiometry

Areal properties of the bilateral proximal humeri were obtained using DXA (Discovery-W machine with Apex v2.3 software; Hologic, Inc., Waltham, MA, USA), as previously described [6]. The subject's shoulder was positioned centrally on the table with care taken to position the humerus vertically within the scan field and a regional scan performed. Bone area (cm^2), BMC (g), and aBMD (g/cm^2) of the proximal humerus were obtained by placing a region of interest over the proximal 25% of the bone with a set width of 80 lines (80.64 mm). The region of interest spanned the humeral head and proximal diaphysis, regions imaged by QCT and MRI. Short-term precision on five individuals scanned five times with interim repositioning showed root mean square coefficients of variation (RMS-CVs) of 1.6%, 3.0%, and 2.8% for proximal humerus bone area, BMC, and aBMD, respectively. A whole-body scan was performed to acquire whole-body aBMD (g/cm^2), lean mass (kg) and percent fat (%), with repeat scans with interim repositioning in 10 individuals yielding RMS-CVs of < 1% for whole-body aBMD and lean mass, and 2.8% for percent fat.

2.3. Quantitative computed tomography

The bilateral humeri were imaged using a multi-slice helical CT scanner (Phillips Brillance 64; Philips Medical Systems, Cleveland, OH) operating at 120 kVp, 400 mAs, 64 × 0.625 collimation, and pitch 0.6. Scan volumes included the entire proximal humerus and included a phantom containing calcium hydroxyapatite standards embedded in water-equivalent resin (Mindways Software, Inc., Austin, TX). Images were axially reconstructed with 1.0 mm slice width spaced 0.5 mm apart using a 768 × 768 matrix and field of view of < 30 cm (reconstructed voxel size < 0.5 × 0.5 × 1.0 mm^3).

Volumetric cortical bone properties were obtained from a tomographic image at 15% distal of humeral length from its proximal end, corresponding to the surgical neck of the proximal humerus. The image was imported into ImageJ v1.45s (National Institutes of Health, Bethesda, MD) and analyzed using the BoneJ plugin [26]. The outer bone edge was segmented with a threshold of 700 mg/cm^3, whereas a threshold of 300 mg/cm^3 separated the cortical and subcortical/trabecular bone compartments, with the linear relationship between Hounsfield Units and known densities of the calcium hydroxyapatite standards used to determine voxel density (mg/cm^3). Parameters obtained were: cortical bone mineral content (Ct.BMC; mg/mm), trabecular/subcortical bone mineral content (Tb.BMC; mg/mm); total area (Tt.Ar; cm^2), cortical area (Ct.Ar; cm^2), medullary area (Me.Ar; cm^2), average cortical thickness (Ct.Th; mm), and polar moment of inertia (I_P; cm^4). Precision for QCT measures was not assessed due to radiation exposure concerns (estimated at 25 mSv per scan or a total of 50 mSv) and because we anticipated throwing-to-nonthrowing differences well beyond measurement error.

2.4. Magnetic resonance imaging

Trabecular bone properties were assessed from coronal high-spatial resolution MR images (Fig. 1A) acquired on a 3T Magnetom Skyra scanner (Siemens Medical Solutions, Erlangen, Germany) using an 8-channel phased array shoulder coil (Invivo, Orlando, FL) and a three-dimensional (3D) constructive interference steady state (CISS) sequence. Acquisition parameters included: repetition time/echo time, 10.73/4.44 ms; flip angle, 60°; slice thickness, 500 μm; and matrix size of 512 × 410. These parameters yielded a voxel resolution of 195 × 195 × 500 μm and acquisition time of 12 min.

Automatic coil-induced intensity inhomogeneity correction by nonparametric nonuniform intensity normalization (N3) was applied [27], and the epiphysis forming the humeral head and greater tubercle was manually delineated 1 mm in from the subcortical bone border and excluding any subchondral cysts (Fig. 1B). Analyses were restricted to the epiphysis as it contained sufficient yellow/fatty marrow for good signal-to-noise ratio. Local bone enhancement fuzzy clustering [28] was applied to segment the trabecular bone within the region of interest (Fig. 1C) and assess the following parameters: bone volume fraction (BVF), trabecular bone number (Tb.N), trabecular bone spacing (Tb.Sp) and trabecular bone thickness (Tb.Th), as previously described by Majumdar and Genant [29] We did not perform repeat scans to determine precision in the current study because of cost; however, triplicate scans in 3 volunteers performed previously by our team at an

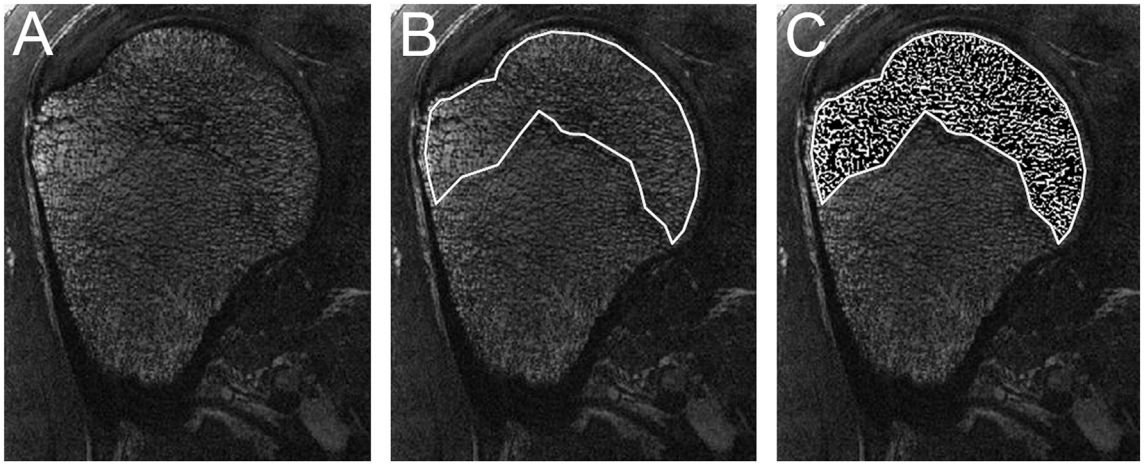

Fig. 1. Assessment of 3D trabecular bone parameters using high-spatial resolution MR imaging. A) Representative acquired coronal cross-sectional image. B) Region of interest delineated within the epiphysis of the humeral head and greater tubercle. C) Trabecular bone segmented within the region of interest. Analyses were performed on all serial slices containing the region of interest.

equivalent deep bone site (e.g. femoral head) yielded RMS-CVs of 3.6% for BVF to 6.2% for Tb.Sp. [30]

2.5. Voxel- and vertex-based analyses

Statistical parametric mapping (SPM) was used to assess localized differences in the spatial distribution of bone properties between throwing and nonthrowing arms. In particular, we used voxel-based morphometry (VBM) to assess for differences in the spatial distribution of vBMD [31], and cortical bone mapping (CBM) to identify regions distributed over the surface of the bone where throwing and nonthrowing arms had different cortical bone thickness (Ct.Th) [32,33] and vBMD in a layer adjacent to the endosteal surface (EndoTb.vBMD) [25]. EndoTb.vBMD provides an indication of endocortical trabecular quantities. Left arm scans were mirrored to those of the right arm, and the segmented bones were spatially normalized to a minimum deformation template (MDT) representing the average size and shape of all proximal humeri in the study. The spatial normalizations reduced the anatomical variability among the humeri, effectively establishing anatomical correspondences locally. The computed transformations were then applied to the vBMD maps and to the surface-based maps of Ct.Th and EndoTb.vBMD, enabling voxel-wise and vertex-wise comparisons between throwing and nonthrowing arms. Registrations to build the MDT and for the spatial normalizations included affine and nonlinear transformations. As reported earlier, we did not perform repeat QCT scans for determination of precision; however, SPM on repeat scans in 22 subjects at an equivalent site (e.g. proximal femur), but where radiation exposure is lower (3 mSv) yielded mean RMS-CVs of 3.5–3.9% and 2.7–3.2% for cortical bone thickness and vBMD, respectively [33].

2.6. Strain energy distribution within the proximal humerus during throwing

Strain energy distribution within the proximal humerus at the time of maximum joint torques during a fast-pitch baseball pitch was modeled in a MLB/MiLB player, as previously described [15]. Three-dimensional MR images (Magnetom Verio; Siemens Medical Solutions, Erlangen, Germany) of muscles attaching to the arm were obtained using a Dixon volumetric interpolated breath-hold examination (VIBE) T1-weighted sequence. Muscles were segmented and their volumes determined. Three-dimensional joint angles at the shoulder and elbow during a fastball pitch were measured at the American Sports Medicine Institute (Birmingham, AL) and inverse dynamics used to calculate net joint torques. Torques were decomposed into individual muscle forces by minimizing the sum of the squares of all muscle stresses [34,35]. The humerus of the throwing arm was segmented from CT data, converted into a three-dimensional solid model (Geomagic v10, Geomagic, Morrisville, NC), and meshed with quadratic tetrahedral elements (Abaqus v11.1, Dassault Systemes, Vélizy-Villacoublay, France). Each element was assigned a Young's modulus based on the x-ray attenuation values and apparent density derived from the calibration phantom.

The muscle and joint reaction forces were applied to the bone surfaces of the finite element model as nodal point loads. The glenohumeral joint reaction force location was calculated as the intersection of the joint reaction force vector passing through the center of the humeral head. Nodes at the center of the olecranon were kinematically constrained to model the elbow joint reaction force. Three nodes on the medial and lateral aspects of the distal humerus were constrained to model ligament forces. A single node at the glenohumeral joint center was used to affix linear spring elements to model the passive soft tissue restraint. A linear stress analysis was performed to calculate the strain energy density. Results from elements within a 4 mm radius of the nodal boundary conditions were neglected to avoid errors resulting from boundary effects. To explore strain energy density distribution in a non-adapted bone, the muscle and joint forces were also applied to a finite element model of the contralateral nonthrowing arm.

2.7. Statistical analyses

Two-tailed analyses with $\alpha = 0.05$ were performed with IBM SPSS Statistics (v24; SPSS Inc., Chicago, IL), unless otherwise specified. Side-to-side differences between the throwing and nonthrowing arms were assessed by calculating mean absolute (throwing − nonthrowing) and mean percent ([throwing − nonthrowing] / nonthrowing × 100%) differences and their 95% confidence intervals (CI). 95% CIs not crossing zero were considered statistically significant, as determined by single sample *t*-tests with a population mean of 0%.

Voxel-wise and vertex-wise differences between the throwing and nonthrowing arms were determined using linear mixed-effects models with a random intercept, allowing for age, height, weight, and shape as follows:

$$\begin{aligned}\text{Bone property} = {} & b0 + b1^{*}\text{Arm} + b2^{*}\text{Age} + b3^{*}\text{Height} + b4^{*}\text{Weight} \\ & + b5^{*}\text{PC1Shape} + b6^{*}\text{PC2Shape} + b7^{*}\text{PC3Shape} \\ & + b8^{*}\text{PC4Shape} + b9^{*}\text{PC5Shape} + (1 \mid \text{Subject}) + \text{error}\end{aligned}$$

where: Bone property = vBMD or Ct.Th or EndoTb.vBMD; Arm = 0 for nonthrowing and 1 for throwing arms; age, height and weight were the same for both arms as comparisons were within-subject; and PC1Shape-PC5Shape were computed for each arm and represented the first 5

Table 1
Demographic and anthropometric characteristics (n = 36)[a].

Characteristic	
Demographics	
Age (yr)	27.7 ± 2.3
Age started throwing (yr)	5.9 ± 2.7
Total years throwing (yr)	21.7 ± 3.7
Playing position (pitcher/catcher)	26/10
Professional (MLB/MiLB) games played (n)	312 ± 218
Professional (MLB/MiLB) innings pitched (n)	617 ± 320
Whole-body anthropometry	
Height (m)	1.87 ± 6.7
Mass (kg)	96.9 ± 8.9
BMI (kg/m^2)	27.8 ± 2.6
aBMD (g/cm^2)[b,c]	1.37 ± 0.08
Lean mass (kg)	64.9 ± 2.7
Fat mass (%)	21.9 ± 4.1

MLB/MiLB = major/minor league baseball.
[a] Data are mean ± SD (except for frequencies).
[b] Values corrected for whole-body lean mass.
[c] Obtained via dual-energy x-ray absorptiometry.

modes of shape [24,36]. The local comparisons performed with the above bone property equation yielded a Student's t-test map (t-Map) for b1 and its corresponding p-value map, which was corrected for multiple comparisons using a false discovery rate (FDR) correction (q = 0.05) [37]. Significant voxels after FDR correction indicated significant differences in vBMD, while significant vertices after FDR correction indicated significant differences in Ct.Th or EndoTb.vBMD between throwing and nonthrowing arms.

3. Results

3.1. Participant characteristics

Demographic and anthropometric characteristics of the 36 MiLB/MLB players recruited are detailed in Table 1. Different numbers of participants were assessed on each imaging modality due to subject and equipment availability, with numbers imaged on each modality detailed in succeeding sections.

3.2. Whole proximal humerus areal bone properties

Proximal humerus areal bone properties were assessed via DXA in 25 players (Table 2). The proximal humerus in throwing arms had 23.5% (95% CI, 14.1 to 33.0%), 28.1% (95% CI, 17.8 to 38.3%) and 3.5% (95% CI, 2.4 to 4.7%) greater aBMD, BMC and area than nonthrowing arms, respectively (all $p < 0.001$) (Fig. 2).

3.3. Volumetric bone properties at the surgical neck

Volumetric bone properties at the surgical neck of the proximal humerus were assessed via QCT in 18 players (Table 2). Images from a representative players are shown in Fig. 3A. The proximal humerus in throwing arms had 35.6% (95% CI, 24.8 to 46.7%) and 89.3% (95% CI, 46.6 to 137.1%) greater bone mass in the cortical (Ct.BMC) and subcortical/trabecular compartments (Tb.BMC) compared to nonthrowing arms, respectively (all $p < 0.01$) (Fig. 3B). The greater mass in the cortical compartment of throwing arms was distributed on the periosteal surface as evidenced by mean throwing-to-nonthrowing arm differences of 12.0% (95% CI, 8.2 to 15.8%) for Tt.Ar ($p = 0.001$), yet no throwing-to-nonthrowing arm differences for Me.Ar ($p = 0.18$) (Fig. 3B). The larger bone size (i.e. Tt.Ar) without a difference on the inner bone area (i.e. Me.Ar) yielded throwing-to-nonthrowing arm differences of 38.9% (95% CI, 27.9 to 49.9%) and 31.0% (95% CI, 17.8 to 44.2%) for Ct.Ar and Ct.Th, respectively (all $p < 0.01$) (Fig. 3B). The mass and structural differences contributed to throwing arms having

Table 2
Proximal humerus properties in the throwing and non-throwing arms.

	Nonthrowing arm[a]	Throwing arm[a]	Absolute diff. (95% CI)[b]
DXA (n = 25)			
aBMD (g/cm^2)	0.938 ± 0.204	1.134 ± 0.208	0.20 (0.11, 0.28)***
BMC (g)	28.9 ± 5.7	36.3 ± 7.0	7.4 (4.5, 10.3)***
Area (cm^2)	31.0 ± 1.9	32.1 ± 2.1	1.1 (0.7, 1.5)***
QCT (n = 18)			
Ct.BMC (mg/mm)	207 ± 28	281 ± 60	74 (49, 98)***
Tb.BMC (mg/mm)	60 ± 33	105 ± 48	45 (34, 56)***
Tt.Ar (cm^2)	7.85 ± 1.08	8.77 ± 1.12	0.92 (0.63, 1.20)***
Ct.Ar (cm^2)	1.92 ± 0.20	2.67 ± 0.54	0.75 (0.52, 0.98)***
Me.Ar (cm^2)	5.93 ± 1.05	6.07 ± 1.09	0.14 (−0.08, 0.36)
Ct.Th (mm)	2.48 ± 0.44	3.22 ± 0.72	0.74 (0.49, 0.98)***
I_P (cm^4)	7.29 ± 1.99	11.25 ± 2.66	3.96 (3.18, 4.74)***
MR imaging (n = 11)			
BVF (%)	37.8 ± 0.7	39.0 ± 0.8	1.2 (0.4, 1.9)**
Tb.Th (mm)	0.282 ± 0.019	0.275 ± 0.011	−0.007 (−0.019, 0.005)
Tb.Sp (mm)	0.462 ± 0.038	0.431 ± 0.026	−0.031 (−0.060, −0.002)*
Tb.N (1/mm)	1.36 ± 0.10	1.43 ± 0.058	0.07 (0.01, 0.14)*

aBMD = areal bone mineral density; BMC = bone mineral content; Ct.BMC = cortical bone mineral content; Tb.BMC = trabecular bone mineral content; Tt.Ar = total area; Ct.Ar = cortical area; Me.Ar = medullary area; Ct.Th = cortical thickness; IP = polar moment of inertia; BVF = bone volume fraction; Tb.Th = trabecular thickness; Tb.Sp = trabecular spacing; Tb.N = trabecular number.
[a] Data are mean ± SD.
[b] Mean absolute differences between throwing and nonthrowing were assessed using single sample t-tests with a population mean of 0. Significance is indicated by: *$p < 0.05$, **$p < 0.01$, ***$p < 0.001$.

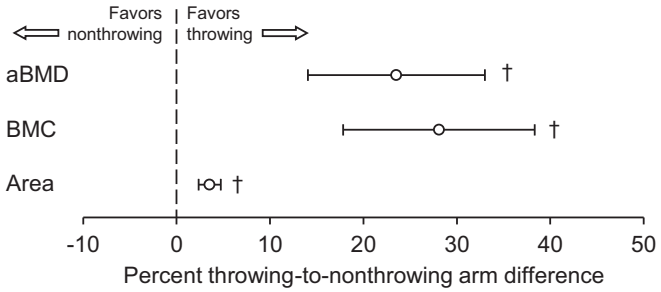

Fig. 2. Effect of throwing-related physical activity on DXA-derived proximal humerus areal bone mineral density (aBMD), bone mineral content (BMC), and bone area. Data represent the mean percent difference between throwing and nonthrowing arms, with error bars indicating 95% confidence intervals. Confidence intervals > 0% indicate greater bone properties within the throwing arm compared to nonthrowing arm (†$p < 0.01$).

56.8% (95% CI, 44.9 to 68.8%) greater estimated ability to resist torsional forces (i.e. I_P) than nonthrowing arms ($p < 0.001$) (Fig. 3B).

3.4. Trabecular bone properties within the humeral head/greater tubercle

Trabecular bone properties within the humeral head and greater tubercle were assessed from MR images in 11 players (Table 2). Throwing arms had 3.1% (95% CI, 1.1 to 5.1%) greater BVF than nonthrowing arms ($p = 0.006$) (Fig. 4). The higher BVF resulted from 5.8% (95% CI, 0.7 to 10.9%) more trabeculae (i.e. Tb.N) in throwing arms compared to nonthrowing arms ($p = 0.03$), as opposed to an increase in size of the trabeculae (i.e. Tb.Th) ($p = 0.21$) (Fig. 4). The presence of more trabeculae in throwing arms reduced the space between trabeculae (i.e. Tb.Sp) by 6.2% (95% CI, 0.1 to 12.3%)

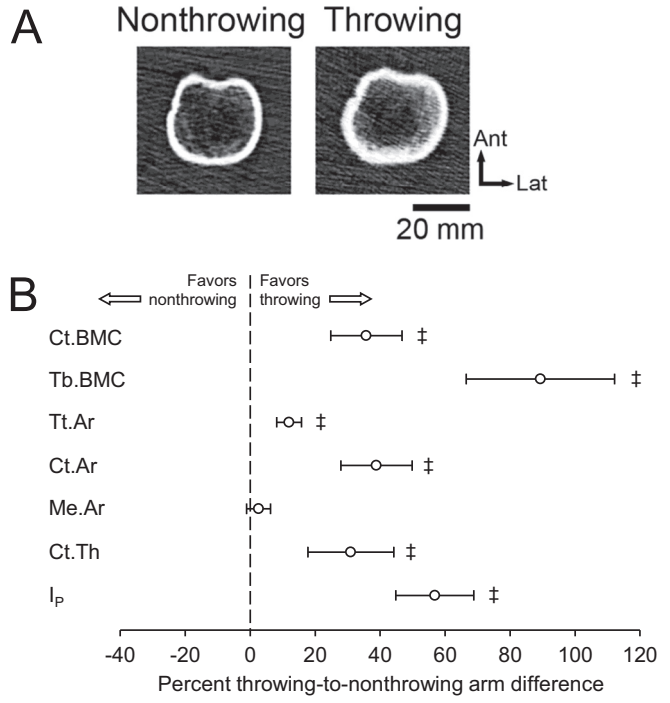

Fig. 3. Effect of throwing-related physical activity on QCT-derived bone properties at the level of the surgical neck of the proximal humerus. A) Tomographic images at the level of the surgical neck in the nonthrowing and throwing arms of a representative individual. Note the larger bone with thicker cortex in the throwing arm. B) The throwing arm had enhanced cortical (Ct.BMC) and trabecular (Tb.BMC) bone mineral content, total bone area (Tt.Ar), cortical area (Ct.Ar), cortical thickness (Ct.Th), and polar moment of inertia (I_P) compared to the nonthrowing arm. There were no side-to-side differences in medullary area (Me.Ar). Data in B) represent the mean percent difference between throwing and nonthrowing arms, with error bars indicating 95% confidence intervals. Confidence intervals > 0% indicate greater bone properties within the throwing arm compared to nonthrowing arm ($^{\ddagger}p < 0.001$).

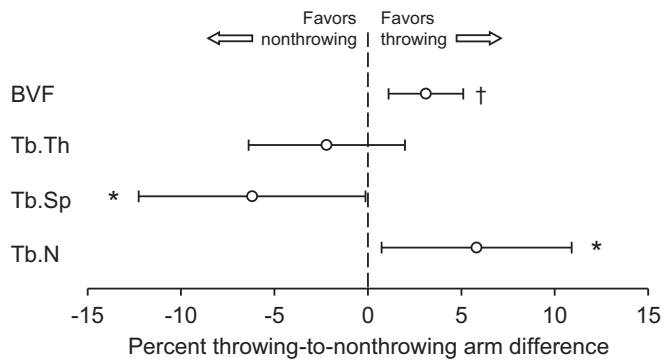

Fig. 4. Effect of throwing-related physical activity on MR imaging-derived trabecular bone properties within the humeral head epiphysis and greater tubercle. Throwing arms had greater bone volume fraction (BVF) and trabecular bone number (Tb.N) than nonthrowing arms and less trabecular bone spacing (Tb.Sp). There were no side-to-side differences in trabecular bone thickness (Tb.Th). Data represent the mean percent difference between throwing and nonthrowing arms, with error bars indicating 95% confidence intervals. Confidence intervals > 0% indicate greater bone properties within the throwing arm compared to nonthrowing arm ($^{*}p < 0.05$ and $^{\dagger}p < 0.01$).

($p = 0.04$).

3.5. Volumetric bone mineral density distribution and cortical bone thickness within the proximal humerus

Three-dimensional t-maps of significant voxel-wise differences in vBMD between throwing and nonthrowing arms in the 18 players imaged via QCT are shown in Fig. 5. Regions with significantly greater vBMD in throwing arms compared to nonthrowing arms (positive t-values) were primarily located in the proximal diaphysis and surgical neck (Fig. 5A and B), with the greatest differences in the posterolateral cortex of the proximal diaphysis (Fig. 5C). In addition, there was a spot of greater vBMD in the posterosuperior aspect of the humeral head in throwing arms (Fig. 5C).

Cortical bone mapping t-maps for significant vertex-wise differences in Ct.Th and EndoTb.vBMD in the proximal diaphysis are shown in Fig. 6. Throwing arms had greater Ct.Th (positive t-values) throughout the majority of the proximal diaphysis compared to nonthrowing arms, with greatest side-to-side differences observed posterolaterally (Fig. 6A). EndoTb.vBMD was also greater (positive t-values) in the posterolateral region of the proximal diaphysis in throwing arms compared to nonthrowing arms (Fig. 6B).

3.6. Strain energy distribution within the proximal humerus during overhead throwing

Strain energy distribution was calculated at the time of maximum shoulder rotation (79.0 Nm) and elbow varus (76.2 Nm) torques, which are over 5 times the torques experienced during everyday tasks [38], and occurred simultaneously at 37 ms prior to ball release during the late cocking phase of the fastball pitch. Applying the subject-specific torques, infraspinatus (2369 N) and the acromial portion of deltoid (2237 N) were calculated to be the principal force generators. Lesser contributions were calculated from the long head of triceps (817 N), teres minor (784 N), clavicular heads of pectoralis major (490 N) and deltoid (437 N), and sternal head of pectoralis major (396 N).

The greatest strain energy distribution was within the posterolateral proximal diaphysis, with 'hot-spots' corresponding to the articulation with the glenoid fossa, and infraspinatus and teres minor muscle insertions (Fig. 7A). When the same forces were applied to the humerus in the player's nonthrowing arm, strain energy density was greater throughout the humeral head and more than doubled within the proximal diaphysis than in the throwing arm (Fig. 7B). The strain energy density also had a different pattern of distribution within the proximal diaphysis of the nonthrowing arm.

4. Discussion

The current data demonstrate the magnitude and site-specific adaptation of the proximal humerus to prolonged, intensive physical activity. Using overhand throwing athletes as an established model of unilateral-dominant upper extremity physical activity [15,39–41], the proximal humerus in throwing arms had over 25% more BMC than contralateral nonthrowing arms when assessed using DXA. These side-to-side differences are approximately double those reported in racquet-sport players [16,17,19–21], confirming extreme proximal humerus adaptation in professional baseball players [15,39]. When assessed tomographically at the level of the surgical neck, the side-to-side differences were additionally impressive, with throwing arms having over a third more cortical bone than measured in nonthrowing arms. The 35.6% throwing-to-nonthrowing arm differences in tomographically-assessed cortical bone mass at the surgical neck is nearly two-thirds greater than racquet-to-nonracquet arm differences (21.7%) reported at the same site in racquet sport players [18].

The additional bone at the surgical neck was principally deposited on the periosteal surface as evident by an enhanced overall bone size

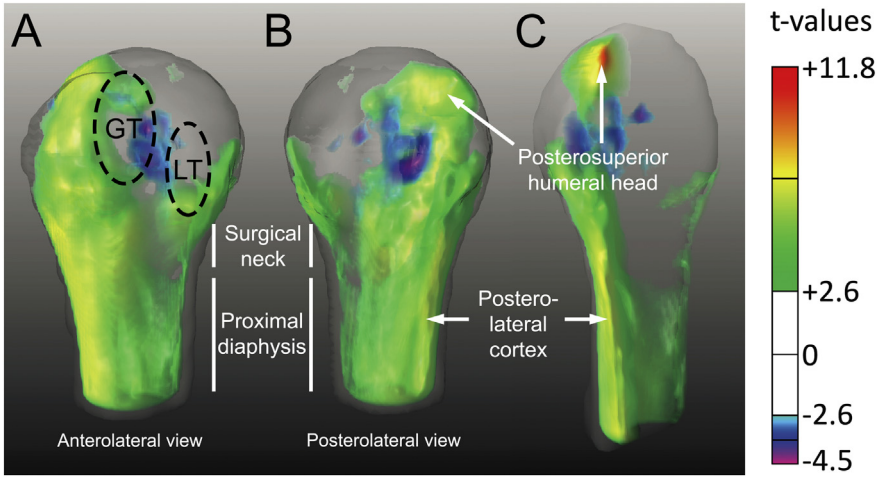

Fig. 5. Anterolateral (A), posterolateral (B) and coronal cut-away (C) views of the 3D t-map showing voxel-wise differences in vBMD between the throwing and non-throwing arms. Voxels with positive and negative t-values indicate significantly higher and lower vBMD in throwing arms compared to contralateral nonthrowing arms, respectively. Voxels where there were no statistical differences between throwing and nonthrowing arms are rendered transparent. GT = greater tubercle; LT = lesser tubercle. Color figure available in online version of article.

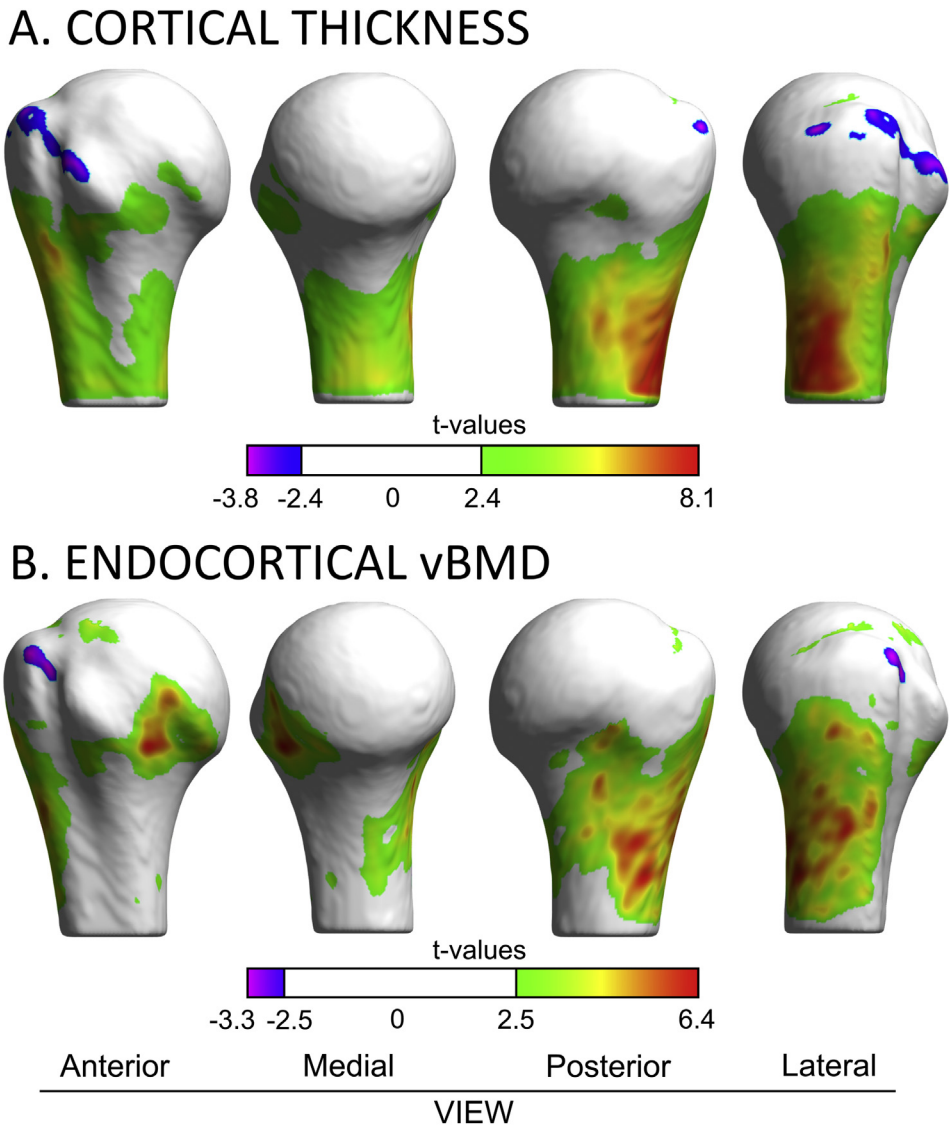

Fig. 6. Surface-based maps of vertex-wise differences between throwing and nonthrowing arms for A) cortical thickness and B) vBMD in the layer adjacent to the endosteal surface within the proximal humeral diaphysis. Vertices with positive t-values indicate significantly greater properties within throwing arms compared to contralateral nonthrowing arms. Vertices where there were no differences between throwing and nonthrowing arms are rendered white. The humeral head was excluded from the analyses due to its thin cortical bone. Color figure available in online version of article.

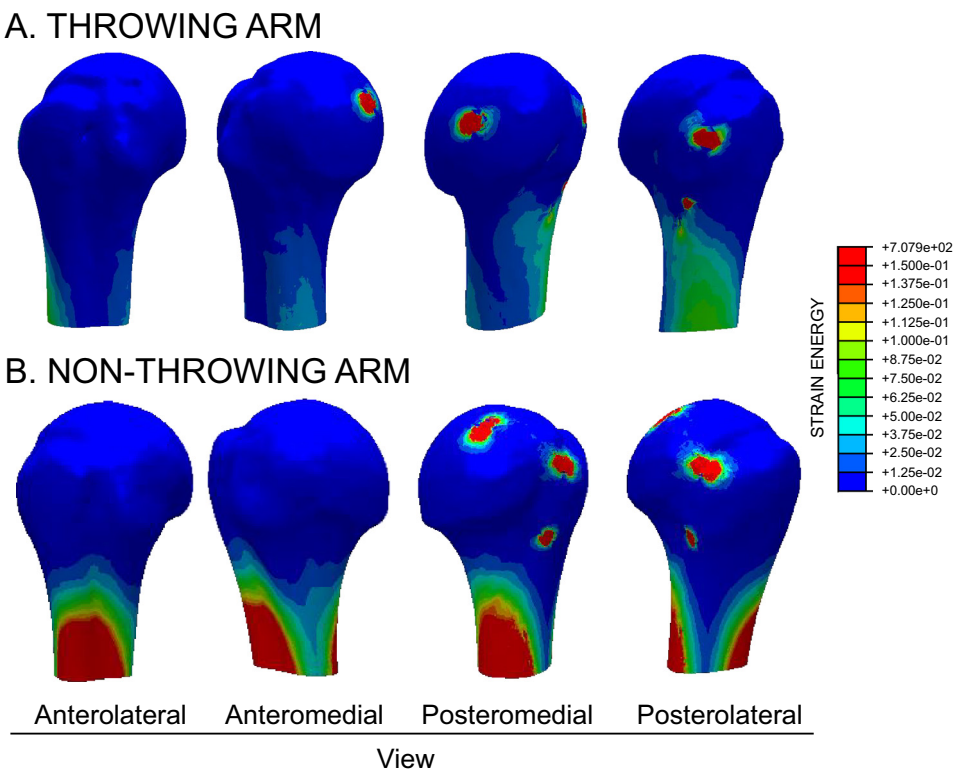

Fig. 7. Strain energy distribution within the proximal humerus at the time of maximum shoulder and elbow torques during a fastball pitch in a MLB/MiLB pitcher. Musculoskeletal model derived forces were applied to finite element models of the humerus in the player's throwing (A) and nonthrowing (B) arm. Applying the forces to the non-adapted nonthrowing arm resulted in more than doubling of the strain energy density and a different distribution pattern within the proximal diaphysis compared to in the adapted throwing arm. Color figure available in online version of article.

without a concomitant change in medullary cavity size. The net result of adding bone at a distance from mechanical axes was a disproportionately greater ability to resist mechanical forces in throwing arms for the amount of mass added. In particular, throwing arms had over 50% greater estimated strength (e.g. I_P) at the level of the surgical neck than measured in nonthrowing arms, with I_P predicting 90% of the variance in the ability of the humeral diaphysis to resist torsional forces [42]. This is a large difference in strength at a fracture prone site, with fractures at the surgical neck of the humerus accounting for half of all proximal humerus fractures [43].

The functional implication of enhanced mechanical properties within the proximal diaphysis and surgical neck regions was evident when strain energy density distribution was modeled in a representative player, who had 59.4% throwing-to-nonthrowing difference in I_P at the level of the surgical neck. Strain energy density within the proximal diaphysis of the throwing arm at the time of maximum shoulder and elbow torques during a fastball pitch was less than half that modeled when the same forces were applied to the contralateral nonadapted arm. In addition, the distribution of strain energy density in the proximal diaphysis of the throwing arm was altered relative to the nonthrowing arm and exhibited a more homogeneous pattern. These data confirm loading-induced mechanoadaptation reduces tissue-level loading to effectively increase the safety factor between functional and injurious loads.

We used high-resolution MR imaging to explore trabecular bone microarchitecture adaptation within the proximal humerus to throwing-related physical activity. Few clinical studies have explored physical activity effects on trabecular bone microarchitecture due to spatial resolution limitations associated with available imaging techniques. The introduction of high-resolution peripheral quantitative computed tomography has partly addressed this issue, but the technique is not amendable to the proximal humerus. Using high-resolution MR imaging, we identified throwing arms possessed more trabecular bone (i.e. BVF) within the epiphyseal region of the humeral head and greater tubercle when compared to nonthrowing arms. The additional bone was from an increased number of trabeculae (i.e. Tb.N) as opposed to their size (i.e. Tb.Th). This pattern of adaptation consisting of an increase in trabeculae number vs. size matches cross-sectional studies that used high-resolution MR imaging to compare trabecular bone health in athletes versus controls [44,45]. However, the functional significance of our observed trabecular bone microarchitecture differences is not clear as throwing-to-nonthrowing differences were small (3.1% for BVF), with previous cross-sectional studies showing athletes (gymnasts and fencers) to have 13.6% and 18.6% greater BVF compared to controls at the proximal tibia and distal femur, respectively [44,45].

The DXA, QCT and MR imaging analyses demonstrated the magnitude of adaptation associated with throwing-related physical activity within the proximal humerus as a whole, and regionally at the level of the surgical neck and within the humeral head. While informative, these generally conventional global and subregional analysis approaches do not provide information on site-specific local patterns. There is growing data suggesting that different osteoporotic fractures can be distinguished by looking at focal alterations in bone health [23–25]. For instance, SPM approaches can classify fracture type (femoral neck vs. trochanteric) at the proximal femur better than DXA-derived measures [23,24]. Similarly, it is increasingly recognized that bone loading and subsequent mechanoadaptation is site-specific not only to the loaded bone, but to specific tissue regions within the bone [46,47]. Thus, it is important to locate the regions within a loaded bone that adaptation specifically occurs and the possible functional implications of the focal adaptation.

Using the SPM approach of VBM to identify voxel-wise differences in vBMD between throwing and nonthrowing arms, we identified throwing arms had enhanced vBMD within the posterosuperior region of the humeral head and much of the proximal diaphysis (including surgical neck region). We hypothesize the adaptation within the posterosuperior region of the humeral head is in response to posterosuperior impingement or 'internal impingement'. The shoulder reaches maximum external rotation of 170–180° while in 90–100° of abduction during the late cocking phase of the overhand throwing motion. In this position, the posterosuperior humeral head approximates and impinges

on the posterosuperior labrum and glenoid rim. The net result can be damage to the undersurface of the rotator cuff tendons, bony changes in the posterosuperior humeral head and glenoid fossa, and damage to the posterosuperior glenoid labrum [48].

The observation of enhanced bone properties within lateral regions of the proximal diaphysis and surgical neck was supported by vertex-wise cortical bone mapping analyses. The latter revealed the proximal diaphysis in throwing arms to have greater Ct.Th and EndoTb.vBMD predominantly in the posterolateral region when compared to non-throwing arms. Adaptation of the lateral region of the proximal diaphysis/surgical neck may be clinically relevant as this region has been reported to have the lowest Ct.Th and endocortical trabecular density in individuals over 60 years of age [49].

The pattern of Ct.Th and EndoTb.vBMD adaptation within the proximal diaphysis approximated the pattern of strain energy distribution within the proximal humerus derived from the musculoskeletal and FE model. The model revealed greatest diaphyseal strain energy within the posterolateral proximal diaphysis of the throwing arm at the time of greatest forces during a fastball pitch in a representative player.

Our study has a number of strengths, including the use of a within-subject controlled model to address selection bias, and the use of a range of novel imaging and analysis techniques to identify global and localized patterns of adaptation. However, the study also possesses a number of limitations. We did not assess females or include a control group, with a portion of the observed side-to-side differences possibly being due to elevated habitual unilateral loading associated with simple arm dominance, particularly the differences observed in trabecular bone microarchitecture. However, analyses of QCT scans of the surgical neck region in 10 age- and sex-equivalent control subjects revealed non-significant dominant-to-nondominant arm differences of < 4% (unpublished data), similar to control data reported by Haapasalo et al. [18] We did not document shoulder injury history in participants, with internal impingement potentially contributing to localized throwing-to-nonthrowing arm differences within the posterosuperior humeral head. Strain energy density was only modeled in a single player and at a single time point during a single pitch type. We modeled the time of most extreme forces, but the model did not take into account loading rate to which bone adaptation is sensitive or loading distribution throughout the different phases of the throwing cycle.

In summary, the current study utilized a variety of novel imaging and analysis techniques to demonstrate the adaptive ability of the proximal humerus to physical activity-related mechanical loads. There was substantial mass, structure and estimated strength adaptation within much of the proximal diaphysis, especially the posterolateral cortex, with the pattern of adaptation approximating the pattern of strain energy distribution during a fastball pitch. Given the unique nature of overhand throwing, it remains to be established how these data translate to exercise prescription to improve localized bone health within the proximal humerus and whether the enhanced properties translate into reduced site-specific osteoporotic fracture risk. However, they provide unique insight into the relationship between prolonged loading and skeletal adaptation at a clinically relevant osteoporotic site.

Acknowledgements

This contribution was made possible by support from the National Institutes of Health (R01 AI125080, R01 AR057336, AR057740, R01 AR068456 and P30 AR072581). The authors have no conflicts of interest.

Author contributions statement

S.J.W. and R.K.F. contributed to study design; all authors contributed to the acquisition, analysis and interpretation of data; S.J.W. drafted the paper; all authors critically revised the paper and approve of its final version.

References

[1] B.O. Sumrein, T.T. Huttunen, A.P. Launonen, H.E. Berg, L. Fellander-Tsai, et al., Proximal humeral fractures in Sweden-a registry-based study, Osteoporos. Int. 28 (2017) 901–907.
[2] C. Bergdahl, C. Ekholm, D. Wennergren, F. Nilsson, M. Moller, Epidemiology and patho-anatomical pattern of 2,011 humeral fractures: data from the Swedish Fracture Register, BMC Musculoskelet. Disord. 17 (2016) 159.
[3] M. Palvanen, P. Kannus, J. Parkkari, T. Pitkajarvi, M. Pasanen, et al., The injury mechanisms of osteoporotic upper extremity fractures among older adults: a controlled study of 287 consecutive patients and their 108 controls, Osteoporos. Int. 11 (2000) 822–831.
[4] J.G. Skedros, A.N. Knight, T.C. Pitts, P.J. O'Rourke, W.Z. Burkhead, Radiographic morphometry and densitometry predict strength of cadaveric proximal humeri more reliably than age and DXA scan density, J. Orthop. Res. 34 (2016) 331–341.
[5] F. Barvencik, M. Gebauer, F.T. Beil, E. Vettorazzi, M. Mumme, et al., Age- and sex-related changes of humeral head microarchitecture: histomorphometric analysis of 60 human specimens, J. Orthop. Res. 28 (2010) 18–26.
[6] S.M. Mantila Roosa, A.L. Hurd, H. Xu, R.K. Fuchs, S.J. Warden, Age-related changes in proximal humerus bone health in healthy, white males, Osteoporos. Int. 23 (2012) 2775–2783.
[7] A.M. Doetsch, J. Faber, N. Lynnerup, I. Watjen, H. Bliddal, et al., Bone mineral density measurement over the shoulder region, Calcif. Tissue Int. 71 (2002) 308–314.
[8] C.M. Sprecher, F. Schmidutz, T. Helfen, R.G. Richards, M. Blauth, et al., Histomorphometric assessment of cancellous and cortical bone material distribution in the proximal humerus of normal and osteoporotic individuals: significantly reduced bone stock in the metaphyseal and subcapital regions of osteoporotic individuals, Medicine 94 (2015) e2043.
[9] J. Mather, J.C. MacDermid, K.J. Faber, G.S. Athwal, Proximal humerus cortical bone thickness correlates with bone mineral density and can clinically rule out osteoporosis, J. Shoulder Elb. Surg. 22 (2013) 732–738.
[10] J.H. Oh, B.W. Song, S.H. Kim, J.A. Choi, J.W. Lee, et al., The measurement of bone mineral density of bilateral proximal humeri using DXA in patients with unilateral rotator cuff tear, Osteoporos. Int. 25 (2014) 2639–2648.
[11] J.L. Kelsey, W.S. Browner, D.G. Seeley, M.C. Nevitt, S.R. Cummings, Risk factors for fractures of the distal forearm and proximal humerus. The Study of Osteoporotic Fractures Research Group, Am. J. Epidemiol. 135 (1992) 477–489.
[12] S.H. Lee, P. Dargent-Molina, G. Breart, EPIDOS Group. Epidemiologie de l'Osteoporose Study, Risk factors for fractures of the proximal humerus: results from the EPIDOS prospective study, J. Bone Miner. Res. 17 (2002) 817–825.
[13] T.V. Nguyen, J.R. Center, P.N. Sambrook, J.A. Eisman, Risk factors for proximal humerus, forearm, and wrist fractures in elderly men and women: the Dubbo Osteoporosis Epidemiology Study, Am. J. Epidemiol. 153 (2001) 587–595.
[14] T.V. Nguyen, J.R. Center, J.A. Eisman, Femoral neck bone loss predicts fracture risk independent of baseline BMD, J. Bone Miner. Res. 20 (2005) 1195–1201.
[15] S.J. Warden, S.M. Mantila Roosa, M.E. Kersh, A.L. Hurd, G.S. Fleisig, et al., Physical activity when young provides lifelong benefits to cortical bone size and strength in men, Proc. Natl. Acad. Sci. U. S. A. 111 (2014) 5337–5342.
[16] H. Haapasalo, P. Kannus, H. Sievanen, A. Heinonen, P. Oja, et al., Long-term unilateral loading and bone mineral density and content in female squash players, Calcif. Tissue Int. 54 (1994) 249–255.
[17] H. Haapasalo, P. Kannus, H. Sievänen, M. Pasanen, K. Unsi-Rasi, et al., Effect of long term unilateral activity on bone mineral density of female junior tennis players, J. Bone Miner. Res. 13 (1998) 310–319.
[18] H. Haapasalo, S. Kontulainen, H. Sievanen, P. Kannus, M. Jarvinen, et al., Exercise-induced bone gain is due to enlargement in bone size without a change in volumetric bone density: a peripheral quantitative computed tomography study of the upper arms of male tennis players, Bone 27 (2000) 351–357.
[19] H. Haapasalo, H. Sievänen, P. Kannus, A. Heinonen, P. Oja, et al., Dimensions and estimated mechanical characteristics of the humerus after long-term tennis loading, J. Bone Miner. Res. 11 (1996) 864–872.
[20] P. Kannus, H. Haapasalo, M. Sankelo, H. Sievänen, M. Pasanen, et al., Effect of starting age of physical activity on bone mass in the dominant arm of tennis and squash players, Ann. Intern. Med. 123 (1995) 27–31.
[21] P. Kannus, H. Haapasalo, H. Sievanen, P. Oja, I. Vuori, The site-specific effects of long-term unilateral activity on bone mineral density and content, Bone 15 (1994) 279–284.
[22] T.L.N. Järvinen, P. Kannus, H. Sievänen, Have the DXA-based exercise studies seriously underestimated the effects of mechanical loading on bone? J. Bone Miner. Res. 14 (1999) 1634–1635.
[23] K.E.S. Poole, L. Skingle, A.H. Gee, T.D. Turmezei, F. Johannesdottir, et al., Focal osteoporosis defects play a key role in hip fracture, Bone 94 (2017) 124–134.
[24] G.M. Treece, A.H. Gee, C. Tonkin, S.K. Ewing, P.M. Cawthon, et al., Predicting hip fracture type with cortical bone mapping (CBM) in the Osteoporotic Fractures in Men (MrOS) Study, J. Bone Miner. Res. 30 (2015) 2067–2077.
[25] A. Yu, J. Carballido-Gamio, L. Wang, T.F. Lang, Y. Su, et al., Spatial differences in the distribution of bone between femoral neck and trochanteric fractures, J. Bone Miner. Res. 32 (2017) 1672–1680.
[26] M. Doube, M.M. Klosowski, I. Arganda-Carreras, F.P. Cordelieres, R.P. Dougherty, et al., BoneJ: free and extensible bone image analysis in ImageJ, Bone 47 (2010) 1076–1079.
[27] J. Folkesson, R. Krug, J. Goldenstein, A.S. Issever, C. Fang, et al., Evaluation of

correction methods for coil-induced intensity inhomogeneities and their influence on trabecular bone structure parameters from MR images, Med. Phys. 36 (2009) 1267–1274.
[28] J. Folkesson, J. Carballido-Gamio, F. Eckstein, T.M. Link, S. Majumdar, Local bone enhancement fuzzy clustering for segmentation of MR trabecular bone images, Med. Phys. 37 (2010) 295–302.
[29] S. Majumdar, H.K. Genant, Assessment of trabecular structure using high resolution magnetic resonance imaging, Stud. Health Technol. Inform. 40 (1997) 81–96.
[30] R. Krug, S. Banerjee, E.T. Han, D.C. Newitt, T.M. Link, et al., Feasibility of in vivo structural analysis of high-resolution magnetic resonance images of the proximal femur, Osteoporos. Int. 16 (2005) 1307–1314.
[31] J. Carballido-Gamio, R. Harnish, I. Saeed, T. Streeper, S. Sigurdsson, et al., Proximal femoral density distribution and structure in relation to age and hip fracture risk in women, J. Bone Miner. Res. 28 (2013) 537–546.
[32] G.M. Treece, A.H. Gee, P.M. Mayhew, K.E. Poole, High resolution cortical bone thickness measurement from clinical CT data, Med. Image Anal. 14 (2010) 276–290.
[33] J. Carballido-Gamio, S. Bonaretti, I. Saeed, R. Harnish, R. Recker, et al., Automatic multi-parametric quantification of the proximal femur with quantitative computed tomography, Quant. Imaging Med. Surg. 5 (2015) 552–568.
[34] B.A. Garner, M.G. Pandy, Estimation of musculotendon properties in the human upper limb, Ann. Biomed. Eng. 31 (2003) 207–220.
[35] T. Yanagawa, C.J. Goodwin, K.B. Shelburne, J.E. Giphart, M.R. Torry, et al., Contributions of the individual muscles of the shoulder to glenohumeral joint stability during abduction, J. Biomech. Eng. 130 (2008) 021024.
[36] A.H. Gee, G.M. Treece, Systematic misregistration and the statistical analysis of surface data, Med. Image Anal. 18 (2014) 385–393.
[37] C.R. Genovese, N.A. Lazar, T. Nichols, Thresholding of statistical maps in functional neuroimaging using the false discovery rate, NeuroImage 15 (2002) 870–878.
[38] I.A. Murray, G.R. Johnson, A study of the external forces and moments at the shoulder and elbow while performing every day tasks, Clin. Biomech. 19 (2004) 586–594.
[39] S.J. Warden, Extreme skeletal adaptation to mechanical loading, J. Orthop. Sports Phys. Ther. 40 (2010) 188.
[40] S.J. Warden, E.D. Bogenschutz, H.D. Smith, A.R. Gutierrez, Throwing induces substantial torsional adaptation within the midshaft humerus of male baseball players, Bone 45 (2009) 931–941.
[41] S.J. Warden, A.M. Weatherholt, A.S. Gudeman, D.C. Mitchell, W.R. Thompson, et al., Progressive skeletal benefits of physical activity when young as assessed at the midshaft humerus in male baseball players, Osteoporos. Int. 28 (2017) 2155–2165.
[42] A.M. Weatherholt, K.G. Avin, A.L. Hurd, J.L. Cox, S.T. Marberry, et al., Peripheral quantitative computed tomography (pQCT) predicts humeral diaphysis torsional mechanical properties with good short-term precision, J. Clin. Densitom. 18 (2015) 551–559.
[43] T. Lind, K. Krøner, J. Jensen, The epidemiology of fractures of the proximal humerus, Arch. Orthop. Trauma Surg. 108 (1989) 285–287.
[44] G. Chang, S.K. Pakin, M.E. Schweitzer, P.K. Saha, R.R. Regatte, Adaptations in trabecular bone microarchitecture in Olympic athletes determined by 7T MRI, J. Magn. Reson. Imaging 27 (2008) 1089–1095.
[45] C.M. Modlesky, S. Majumdar, G.A. Dudley, Trabecular bone microarchitecture in female collegiate gymnasts, Osteoporos. Int. 19 (2008) 1011–1018.
[46] R.K. Fuchs, M.E. Kersh, J. Carballido-Gamio, W.R. Thompson, J.H. Keyak, et al., Physical activity for strengthening fracture prone regions of the proximal femur, Curr. Osteoporos. Rep. 15 (2017) 43–52.
[47] M.E. Kersh, S. Martelli, R. Zebaze, E. Seeman, M.G. Pandy, Mechanical loading of the femoral neck in human locomotion, J. Bone Miner. Res. 11 (2018) 1999–2006.
[48] C.K. Fessa, A. Peduto, J. Linklater, P. Tirman, Posterosuperior glenoid internal impingement of the shoulder in the overhead athlete: pathogenesis, clinical features and MR imaging findings, J. Med. Imaging Radiat. Oncol. 59 (2015) 182–187.
[49] Y. Wang, J. Li, J. Yang, J. Dong, Regional variations of cortical bone in the humeral head region: a preliminary study, Bone 110 (2018) 194–198.